ELSEVIER

Chemical Engineering Journal 125 (2007) 165–176

Chemical Engineering Journal

www.elsevier.com/locate/cej

Study on a novel POM-based magnetic photocatalyst: Photocatalytic degradation and magnetic separation

Wei Qiu [a], Ying Zheng [a,*], Katy A. Haralampides [b]

[a] *Department of Chemical Engineering, University of New Brunswick, 15 Dineen Drive, Fredericton, New Brunswick E3B 5A3, Canada*
[b] *Department of Civil Engineering, University of New Brunswick, 17 Dineen Drive, Fredericton, New Brunswick E3B 5A3, Canada*

Received 23 February 2006; received in revised form 25 July 2006; accepted 24 August 2006

Abstract

The photocatalytic performance of a novel polyoxometalate (POM)-based magnetic photocatalyst was studied by photocatalytic degradation of a model compound (formic acid) in an annular fluidized bed photoreactor. Degradation rate, apparent quantum efficiency, and energy efficiency were evaluated and compared with suspended TiO_2 fine particles (Degussa P25) and quartz sand supported TiO_2 photocatalysts. All degradation experiments were conducted under fully irradiated photoreaction (FIP) conditions. Results showed that this novel POM-based magnetic photocatalyst exhibited 2.7–4.2 times higher initial degradation rate and 2.7–3.8 times higher apparent quantum efficiency than the quartz sand supported TiO_2 photocatalyst, depending on the pH of the solution. Though it had lower degradation efficiency and apparent quantum efficiency than suspended P25, it was proved that this POM-based magnetic photocatalyst could be efficiently separated from treated water by high-gradient magnetic separation (HGMS), while the separation for P25 fine particles is quite difficult. The magnetic field/gradient in a lab-constructed HGMS was modeled and simulated by finite element analysis (FEA) to examine the particle capture feasibility. Experimental results proved that separation efficiency higher than 90.1% could be achieved under investigated conditions, i.e., flow velocity lower than 1.375 mm s^{-1} under the studied magnetic photocatalyst concentration.

Keywords: Magnetic photocatalyst; Photocatalytic degradation; Finite element analysis; Magnetic separation

1. Introduction

TiO_2 has been studied extensively as a semiconductor photocatalyst in the last two decades for its good activity, chemical inertness, and low cost [1]. However, given the difficulty in the separation of suspended TiO_2 fine particles from treated water [2], TiO_2 is usually immobilized onto substrates for practical use, known as supported TiO_2 photocatalyst. A significant loss of activity was generally reported due to greatly reduced surface area after immobilization [3].

Magnetic photocatalysts provide an alternative solution for the above problems. With magnetic cores, the submicron-sized magnetic photocatalysts can be recovered from treated water by properly employing an external magnetic field. Compared to conventional supported TiO_2 photocatalysts, the submicron sizes of the magnetic photocatalyst provide a larger surface area, which subsequently enables higher efficiency in photocatalytic degradations. Beydoun et al. [4–6] have conducted a series of pioneer researches in the development of magnetic photocatalysts.

A novel POM-based magnetic photocatalyst was synthesized in the previous work [7]. In this study, degradation experiments were carried out to investigate the photocatalytic performance of this magnetic photocatalyst. As the most widely studied photocatalyst, suspended TiO_2 (Degussa P25) and quartz sand supported TiO_2 photocatalysts were also studied for their photocatalytic performance and compared with the magnetic photocatalyst by the degradation of formic acid solution in a fluidized bed photoreactor.

As an efficient method for the recovery of submicron-sized magnetic particles from water [8–10], high-gradient magnetic separation (HGMS) was first introduced in this study to separate magnetic photocatalyst particles from treated water. In the lab-constructed HGMS, high magnetic field gradients are generated by the fine-grade stainless steel wires packed in the separation chamber that is in a strong external magnetic field exerted by a series of permanent magnets. The high magnetic field gradient is essential for the magnetic traction force to compete with

* Corresponding author. Tel.: +1 506 447 3329; fax: +1 506 453 3591.
E-mail address: yzheng@unb.ca (Y. Zheng).

1385-8947/$ – see front matter © 2006 Elsevier B.V. All rights reserved.
doi:10.1016/j.cej.2006.08.025

Nomenclature

B_r	residual magnetic flux density (T)
C	concentration of formic acid in solution (mg l^{-1} or ppm)
C_0	initial concentration of formic acid in solution (mg l^{-1})
d	diameter of particle (m)
F_d	fluid drag force (N)
F_m	magnetic traction force (N)
h	Planck constant (J s^{-1})
H	magnetic field intensity (A m^{-1})
I_{in}	incident UV-flux intensity
I_{out}	remnant UV-flux intensity
k	reaction rate constant (mg l^{-1} s^{-1})
k_a	apparent reaction rate constant
K	adsorption coefficient of reactant (mg^{-1} l)
M	mass magnetization (A m^2 kg^{-1})
N_a	Avogadro's number
P_{in}	incident power of UV irradiation (W)
P_{out}	remnant power of UV irradiation (W)
r_d	initial degradation rate of formic acid (mol l^{-1} s^{-1})
r_{ph}	photon absorption rate (einstein l^{-1} s^{-1})
t	reaction time (min)
u	velocity of particles related to fluid (m s^{-1})
V_p	volume of particle (m^3)

Greek letters

η	quantum efficiency
η_a	apparent quantum efficiency
μ	viscosity of fluid (kg m^{-1} s^{-1})
μ_r	relative permeability
μ_0	vacuum permeability (kg m s^{-2} A^{-2})
υ	frequency of incident irradiation (s^{-1})
Φ_s	separation efficiency

Abbreviations

I.D.	inner diameter (mm)
$L \times W \times$ Th	length × width × thickness (mm)
O.D.	outer diameter (mm)

the gravity, diffusion, and fluid drag forces exerted on particle. In this work, finite element analysis (FEA) was also employed to simulate the magnetic field distribution and generated magnetic field gradient in the HGMS separation chamber. Both the experimental and simulation results were used to examine the separation feasibility of the POM-based magnetic photocatalysts from water using HGMS.

2. Experimental

2.1. Materials and methods

The POM-based nano-magnetic photocatalyst was prepared in three steps, which are described elsewhere [7]. The POM species used in the synthesis was phosphotungstic acid hydrate ($H_3PW_{12}O_{40}{\cdot}xH_2O$, reagent grade, Sigma–Aldrich). The synthesized POM/Ag/Fe_3O_4 composite possessed a nanosized Fe_3O_4 core with a Ag nanoshell upon which POM anions are attached. The amount of deposited POM was 10.1%, which was determined from the weight percentage measurements of W, Fe and Ag in the synthesized photocatalyst [7]. The weight percentages of W, Fe and Ag were determined by inductively coupled plasma (ICP).

Aeroxide® TiO_2 P25 (average particle size: 21 nm, Degussa) was used as received. Supported TiO_2 photocatalysts used quartz sands (+50–70 mesh, Sigma–Aldrich) as supports and TiO_2 was immobilized onto quartz sands by following an in situ sol–gel coating method [11].

2.2. Characterization

Specification data of Degussa P25 was provided by manufacturer. The surface morphology of quartz sand supported TiO_2 photocatalysts was characterized by scanned electron microscopy (SEM) on a JEOL JSM6400 Digital SEM. The average size of magnetic photocatalyst particles and P25 fine particles in water solution was measured by dynamic light scattering (DLS) on Mastersizer 2000 (optical unit, Malvern) and Hydro 2000S (sampler unit, Malvern). The DLS measurements were conducted in an air-conditioned room, which had a temperature of 25.0 ± 2.1 °C as we monitored by a digital-display thermometer installed on a pH meter (Acumet 3000, Fisher). Magnetization property of synthesized magnetic photocatalyst was tested on a Quantum Design 9T-PPMS dc magnetometer/ac susceptometer.

2.3. Degradation experiments

8.5 l of formic acid solution (200 ppm) was used as the model wastewater in our study. Formic acid was chosen as the model contaminant to simplify the evaluation of quantum efficiency as it oxidizes to CO_2 and H_2O with no intermediates. A blank experiment was conducted without using photocatalyst to determine the decomposition fraction of formic acid under UV irradiation. For the photocatalytic oxidation, 0.20 g P25 powder was added in the water solution, followed by sonication for 3 min at 200 W. For supported TiO_2, approximately 0.20 g TiO_2 was coated on 200 g quartz sands, which gave a ratio of 1 mg TiO_2 g^{-1} quartz sands to obtain a monolayer of TiO_2 on quartz sand surfaces [3]. 1.04 g of POM-based magnetic photocatalyst particles were used to investigate the photocatalytic degradation performance of the synthesized magnetic photocatalyst. The pH of solution was adjusted by adding chlorhydric acid to investigate the photocatalytic activity of POM-based magnetic photocatalyst at different pH levels.

The schematic experimental set-up was shown in Fig. 1. The integrated photoreactor-separator system consists of an annular fluidized bed photoreactor and a HGMS. The photoreactor consists of two coaxial cylindrical columns (effective irradiation length: 640 mm), including the outer acrylic resin column (I.D. 102 mm; O.D. 108 mm) and the inner quartz tube (I.D. 45 mm;

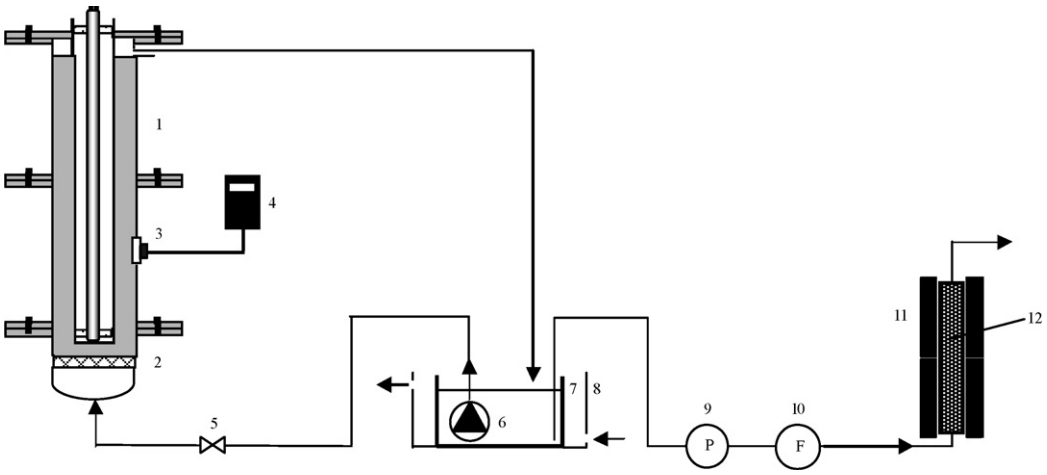

Fig. 1. Photocatalytic experimental set-up: (1) photoreactor, (2) liquid distributor, (3) monitoring window, (4) UV-intensity radiometer, (5) valve, (6) submerged pump, (7) water tank, (8) cooling jacket, (9) peristaltic pump, (10) flowmeter, (11) NdFeB magnet blocks and (12) fine stainless steel wires.

O.D. 48 mm). A 15 W germicidal lamp (254 nm, Spectroline Inc.) was fixed at the axis of inner quartz tube. This configuration is reported to enable a most efficient use of UV irradiation in immersion-type photochemical reactions [12]. A quartz wafer (diameter: 50.8 mm, 4 mm thick, Cole–Parmer) was mounted on the outer wall of reactor as the monitoring window for remanent UV-flux intensity. A fully irradiated condition was assured for all degradation experiments by detecting remnant UV intensity at the quartz wafer using a UV radiometer (254 nm, Cole–Parmer). P25 and magnetic photocatalyst suspensions were continuously pumped into the photoreactor and circulated between the photoreactor and water reservoir at the same flow rate. Quartz sand supported TiO_2 particles were fluidized to the top of the reactor by using a particle-tolerable submerged pump (0.18 kW, Mastercraft Inc.). Treated water samples were collected at the set time intervals during the degradation. The concentration of formic acid was determined by measuring the TOC (total organic carbon) of the treated water samples. The measurements were conducted on a PC-controlled total carbon analyzer (TOC–VCPH, Shimazu).

2.4. Magnetic separation

The magnified scheme of separation unit is shown in Fig. 2. It consists of a thin-wall acrylic resin container (inner dimensions: $L \times W \times \mathrm{Th} = 80.0\,\mathrm{mm} \times 40.0\,\mathrm{mm} \times 20.0\,\mathrm{mm}$) and four NdFeB magnet blocks ($B_r = 1.2\,\mathrm{T}$, $L \times W \times \mathrm{Th} = 50.8\,\mathrm{mm} \times 50.8\,\mathrm{mm} \times 25.4\,\mathrm{mm}$, Master Magnetics Inc.). Each side of the container was fully covered by two NdFeB magnets. The inner space of container was fully packed with fine-grade stainless steel wires (type 430 stainless steel, relative permeability $\mu_r = 409$, diameter: 50 μm). After two batches of degradation experiments, treated water was added together and neutralized then pumped into the HGMS by a peristaltic pump (Fisher-

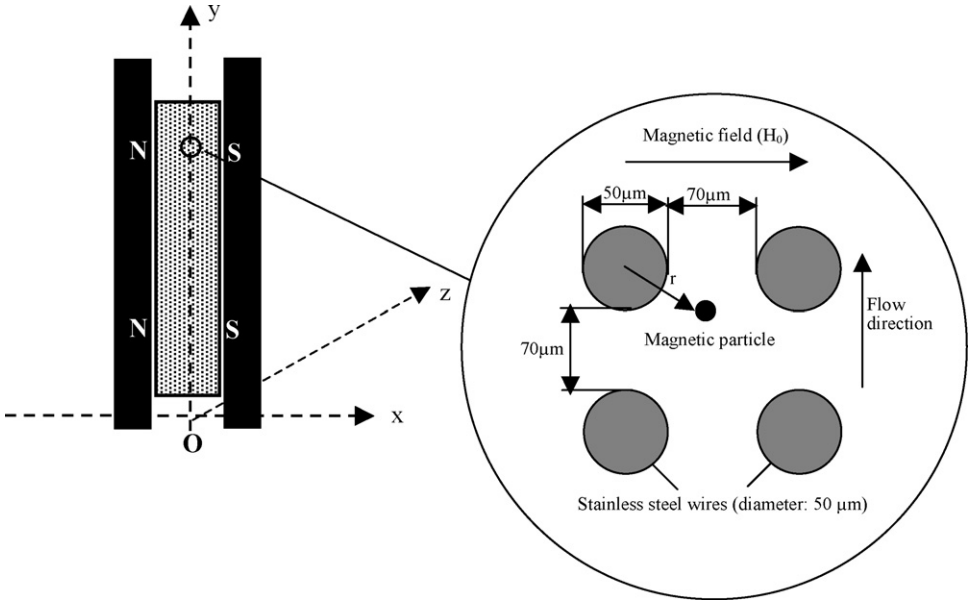

Fig. 2. Scheme of the lab-constructed HGMS.

brand, Fisher). The flow rate was adjusted by a valve-integrated flowmeter. The term "separation efficiency (Φ_s)" was defined as the ratio of "suspended particle concentration (SPC)" in treated water after the separation to the SPC before the separation. Suspended particle concentration (SPC) was estimated by a previously used turbidity-SPC method [13]. Water samples were taken at the time interval of 10 min for the turbidity measurement. After separation, magnets were removed and the separation chamber was flushed by clean water.

3. Theory and modeling

3.1. Definitions and models

The photocatalytic degradation follows a pseudo-first-order kinetics, in agreement with a generally suggested Langmuir–Hinshelwood model [14,15], which is presented as:

$$r_d = \frac{dC}{dt} = \frac{k\,KC}{1 + KC} \tag{1}$$

when C is in millimolar scale (4.3 mmol l^{-1} in this study), Eq. (1) is simplified to an apparent first-order equation as $KC \ll 1$ [14], which is:

$$\ln\left(\frac{C_0}{C}\right) = kKt = k_a t \tag{2}$$

Eq. (2) suggests that a plot of $\ln(C_0/C)-t$ should represent a straight line. The slope upon linear regression determines the apparent first-order rate constant k_a. Initial degradation rate is subsequently obtained from Eq. (1), once k_a and initial concentration C_0 are known.

3.2. Quantum efficiency

Quantum efficiency (η) gives a common ground to compare the efficiency for different photochemical reactions involving different photocatalysts or reactor configurations. As defined in literature [16,17], quantum efficiency equals the ratio of the reaction rate of reactants (mol l^{-1} s^{-1}) to the photon absorption rate (einstein l^{-1} s^{-1}), where an Einstein equals a mol of photons. Since reaction rate is dependant on time, initial quantum efficiency is obtained when the reaction rate term is specified as initial reaction rate:

$$\eta = \frac{\text{reaction rate}}{\text{photon absoprtion rate}} = \frac{r_d\ (\text{mol}\,l^{-1}\,s^{-1})}{r_{ph}\ (\text{Einstein}\,l^{-1}\,s^{-1})} \tag{3}$$

It should be noted that, when a photon travels into the reaction space, scattering, reflection, and absorption of photons occur simultaneously. Only these photons absorbed by photocatalysts can induce the photocatalytic reaction. In heterogeneous photocatalysis, the extent of light scattered and reflected by the particles varies with the reactor geometry and reaction conditions and may reach 13–76% of the total incident photon flow [17]. However, one particular difficulty in quantum efficiency evaluation is the measurement of photons that are actually absorbed by photocatalysts. Thus, the term "apparent quantum efficiency" (η_a) was defined and has been widely accepted in photocatalysis studies [3,18–21], in which researchers neglected scattering and reflection loss of photons to simplify the analysis and only focused on the yield of the process. The apparent quantum efficiency is defined by the following equation:

$$\eta_a = \frac{\text{reaction rate}}{\text{incident photon rate} - \text{remnant photon rate}} = \frac{r_d\ (\text{mol}\,l^{-1}\,s^{-1})}{(P_a\%P_{in})/(h\nu N_a)(\text{einstein}\,l^{-1}\,s^{-1})} \tag{4}$$

where P_a is apparent power capture and calculated by the following equation:

$$\text{Apparent power capture, } P_a\% = \frac{P_{in} - P_{out}}{P_{in}} \times 100 \tag{5}$$

3.3. Energy efficiency

Except for quantum efficiency, one of the practical yardsticks in an industrial environment is the energy efficiency, which describes the efficiency of a given process to determine its economic viability [17]. The energetic efficiency of degradation (EED) is defined as the ppm of degraded organic carbon in a solution irradiated per kW h of electrical energy used. EED enables a broad comparison applicable in different water pollutant degradation processes involving different reactors, light sources, etc. The EED comparison is a useful parameter in economic analysis of various given water pollutant degradation processes. In this study, EED is evaluated and compared for degradation processes by using different types of photocatalysts.

3.4. Magnetic separation

For permanent magnets, an equation was suggested by manufacturers to calculate the magnetic field along the axis [22,23]. For a single rectangular piece of permanent magnet, the magnetic field along its axis is determined by the following equation [23]:

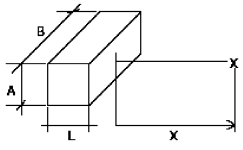

$$H_x = \frac{B_r}{\pi\mu_0\mu_r}\left\{\tan^{-1}\frac{AB}{2X(4X^2 + A^2 + B^2)^{1/2}} - \tan^{-1}\frac{AB}{2(L+X)[4(L+X)^2 + A^2 + B^2]^{1/2}}\right\} \tag{6}$$

where A, B, L are dimensions of magnet and X is the distance away from the magnet along the axis. For identical magnets facing each other in attracting positions, at a point P on the axis between two magnets, H_P is the sum of $H_{(x+p)}$ and $H_{(x-p)}$.

In this study, the relative permeability (μ_r) of water and resin was assumed to be unity [24] and $B_r = 1.2$ T is provided by the manufacturer.

Fine stainless steel wires were packed in the separation chamber to generate high magnetic field gradients. When the external magnetic field (H_x in Eq. (6)) is applied, these magnetically susceptible wires dehomogenize the magnetic field and produce high magnetic field gradients to attract fine magnetic particles. Models have been presented to calculate the magnetic field gradient in HGMS [25–27]. For a wire perpendicular to the external magnetic field (H_0), the generated magnetic field is calculated by [27]:

$$H_r = \left(\frac{M_{wire}a^2}{2r^2} + H_0\right) \tag{7}$$

Thus, the generated magnetic field gradient around wires was:

$$\frac{dH_r}{dr} = -\frac{M_{wire}a^2}{r} \tag{8}$$

where H_r is the magnetic field intensity at the distance r away from the wire, M_{wire} the mass magnetization of wire, a the diameter of the wire and H_0 is the external magnetic field. According to the magnetization curve (available in the built-in materials library of FEMM 4.0), the mass magnetization (M_{wire}) of Type 430 stainless steel has already reached saturation under the applied magnetic filed in our study.

For a successful capture of magnetic photocatalyst particles, magnetic traction force should be dominant among all the forces exerted on particles including gravitational, diffusion, and fluid drag force. Two assumptions are made before further investigation. First, the diffusion force is negligible. It was reported [28] that diffusion of particles should be taken into account only when particle size is less than 40 nm. As indicated by DLS measurements (Fig. 3), the average size of magnetic photocatalyst particles is 650 nm due to their aggregation in water. Second, the interaction between particles is negligible due to the low particle concentration. In addition, the gravitational force could also be neglected since it has a magnitude 10^{-3} lower than fluid drag force in terms of estimation. Therefore, the feasibility of particle capture is determined by the competition between magnetic traction force and fluid drag force. In an external magnetic field, the traction force on magnetic particles is calculated by:

$$F_m = \mu V_p M_p \nabla H \tag{9}$$

where V_p is the volume of particle and M_p is the mass magnetization of magnetic photocatalyst particles. The last term ∇H stands for the magnetic field gradient (H). Generally, μ is the expressed by μ_r the multiplied by μ_0. Since μ_r of water approximately equals to 1, the permeability of water can be simplified as μ_0. Simplified as a 2D static magnet field, the magnetic force was calculated by:

$$F_m = \mu_0 V_p M_p \frac{dH_r}{dr} \tag{10}$$

On the other hand, the drag force on the magnetic particles is calculated by Stokes' Law. When Reynolds number is in the region of 10^{-4} to 0.2, the drag force on a spherical particle is

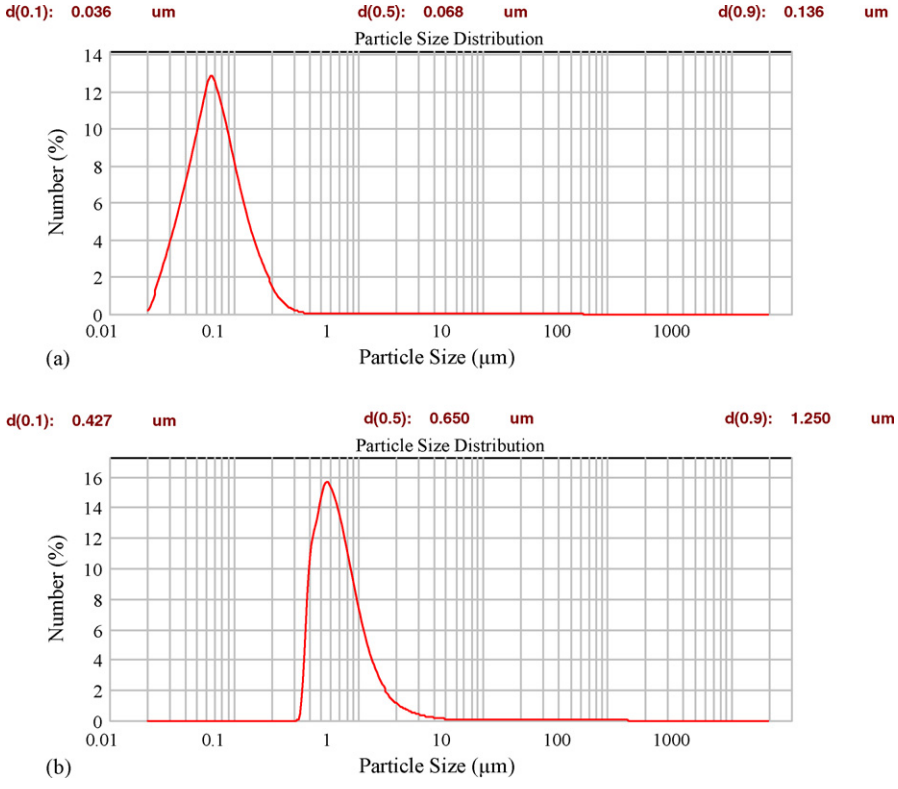

Fig. 3. DLS results: (a) P25 and (b) POM-based magnetic photocatalyst.

expressed by:

$$F_d = 3\pi\mu\, du \tag{11}$$

Similarly, several assumptions have been made to make it applicable in our system. First, particles are assumed to be spherical. Second, there is no relative motion between particles and fluid in the flow direction (*y*-direction, Fig. 2). The relative motion only occurs in *x*-direction.

4. Results and discussion

4.1. Photocatalysts

According to the specification data [29], P25 has 75% anatase, an average particle size of 21 nm, and a specific surface area of $50 \pm 15\ m^2\ g^{-1}$. The size of P25 particle aggregates in water solution was measured by DLS and shown in Fig. 3(a). Results show that P25 particles are in good dispersion in water solution that these particles had an average size of 68 nm.

Fig. 3(b) shows the magnetic photocatalyst particles have an average size of 650 nm due to their aggregation in water. A typical magnetization curve of paramagnetic materials was observed for the synthesized magnetic photocatalyst, as shown in Fig. 4. The magnetization of particles increased sharply as the external magnetic field increased from 0 to $3 \times 10^5\ A\ m^{-1}$. Then the increasing trend slows down when the external magnetic field is higher than $1 \times 10^6\ A\ m^{-1}$, under which the particle's mass magnetization reached its saturation value of $46.1\ A\ m^2\ kg^{-1}$.

The surface morphology of bare quartz sand and quartz sand supported TiO_2 is shown in Fig. 5(a) and (b), respectively. It was observed that bare quartz sand has a relatively rough surface, which is favorable for TiO_2 attachment. Fig. 5(b) shows that TiO_2 was immobilized on quartz sand surface via sol–gel coating method. It was also observed that TiO_2 agglomerated into lumps on the surface at the loading ratio of TiO_2 and quartz sand (1 mg $TiO_2\ g^{-1}$ quartz sand).

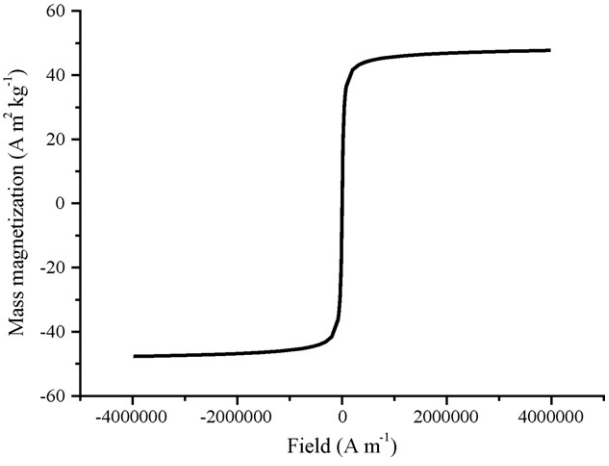

Fig. 4. Magnetic hysteresis loop of magnetic photocatalyst particles.

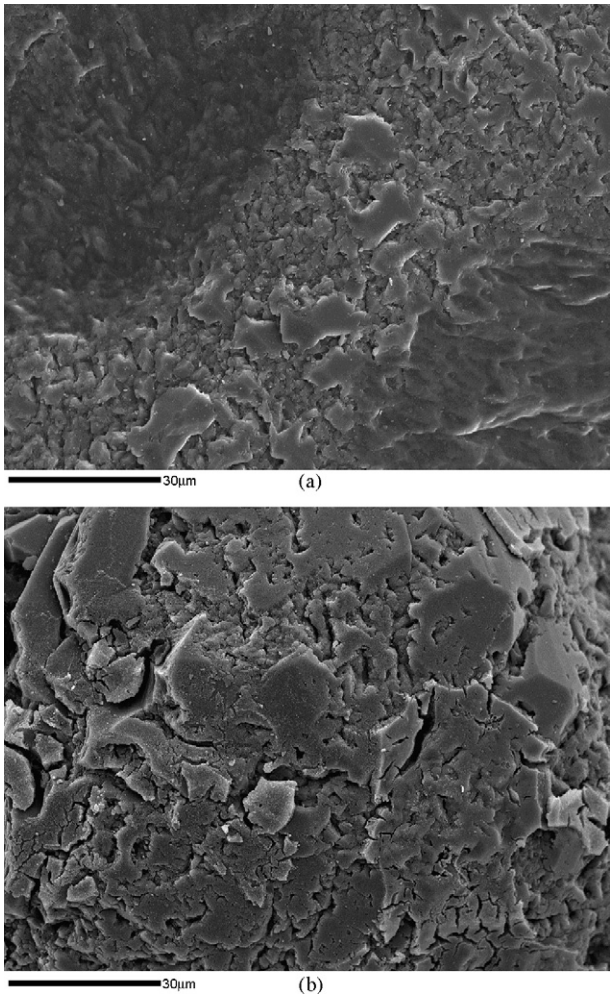

Fig. 5. SEM images: (a) bare quartz sand and (b) quartz sand supported TiO_2 (monolayer).

4.2. Degradation rate, quantum efficiency and energy efficiency

The mineralization of formic acid by direct photolysis was determined by the blank experiment. It was found that, under the experimental conditions, the formic acid in the solution mineralized 3.7% of its initial concentration (from 205.6 to 198 ppm) after 2 h UV-irradiation. This photolysis fraction was deducted from the total degradation percentage to investigate the effect of photocatalytic degradation. Degradation result of each photocatalyst is shown in Fig. 6. Initial concentration of formic acid solution was kept at 200 ppm for all degradation experiments. The performance of POM-based magnetic photocatalyst at different pH levels is also presented.

The time evolution of $\ln(C_0/C)$ shows linear trends in all degradation experiments, which suggests a pseudo-first-order kinetics. The observed pseudo-first-order kinetics is consistent with results in other photocatalytic degradation studies [14,15,30]. The apparent reaction constant (k_a) of each degradation was obtained by linear fitting. Corresponding initial reaction rates were subsequently obtained. Table 1 shows the results of apparent reaction constants and initial reaction rates. As it shows,

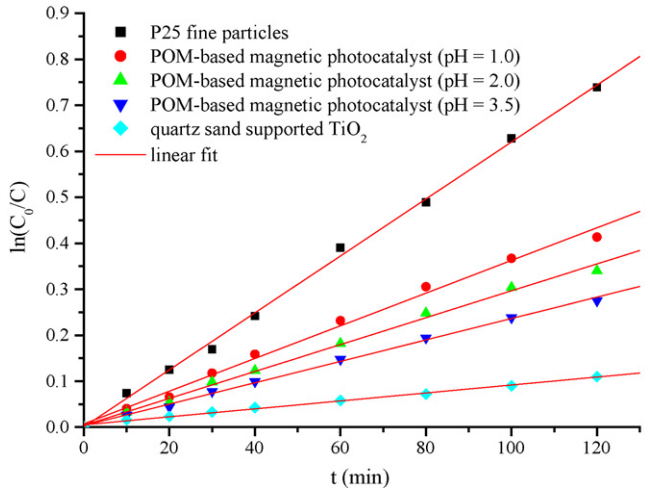

Fig. 6. Degradation results (8.5 l 200 ppm formic acid, 2 h degradation, P25: 0.20 g, supported TiO_2: 0.20 g TiO_2 supported on 200 g quartz sands and POM-based magnetic photocatalyst: 1.04 g).

P25 fine particles exhibit the highest initial degradation rate, which is 7.2 times faster than that of supported TiO_2 photocatalyst. A comparison study carried out by Pozzo et al. [19] also found that the degradation efficiency of P25 fine particles was remarkably lowered by a factor of five times after immobilization. The activity loss of TiO_2 could be ascribed to the decreased surface area of catalyst after immobilization and the lower activity of sol–gel synthesized TiO_2 due to the 450 °C calcination involved in the immobilization of TiO_2 [31].

As seen from Fig. 6, POM-based magnetic photocatalyst shows intermediate degradation efficiency between P25 and quartz sand supported TiO_2. The degradation efficiency of magnetic photocatalyst is higher than the quartz sand supported TiO_2 by a factor of 2.5–3.6 but generally lower than P25 fine particles. Apparently, the submicron aggregates 650 nm of magnetic photocatalyst provide a much larger surface area than that of the quartz sand supported TiO_2. This greater surface area resulted in a significant increase in the photocatalytic efficiency of POM by providing more contact area between the catalyst and the contaminant for the oxidation reactions to take place.

Compared to P25, POM-based magnetic photocatalyst exhibited lower degradation efficiency. Two factors should be taken into account for this lower degradation efficiency. First, as indicated in the DLS results (Fig. 3), the magnetic photocatalyst particles showed serious aggregations in water: an average aggregate size of 650 nm is observed while P25 particles mainly maintain a good dispersion condition. The larger surface area provided by P25 particles was favorable for the contact with contaminant molecule and the exposure under UV-irradiation, both of which contribute to improve the degradation efficiency. Moreover, POM has an inherently lower activity than TiO_2 in photocatalytic degradation due to their different degradation kinetics. A comparison study of $PW_{12}O_{40}^{3-}$ and TiO_2 conducted by Kim et al. [32] indicated that OH radicals were the sole dominant photo-oxidant in POM-mediated degradations whereas both OH radicals and direct hole transfers took part in TiO_2 photocatalysis. Hu and Xu [33] reported similar result that pure POM anions showed lower degradation efficiency than suspended P25. In this study, POM anions were immobilized on Ag/Fe_3O_4 composites to prepare the POM-based magnetic photocatalyst. The lower photocatalytic activity of POM than P25 would also induce the lower degradation efficiency in the POM photocatalyzed degradation than P25 slurry system. Though it was reported that [7,34] the immobilization of POM onto certain supports could effectively enhance its activity, the improvement was probably limited due to the relatively lower specific surface area (96 $m^2\ g^{-1}$) of the Ag/Fe_3O_4 composite.

Table 1
Results of apparent reaction constant and initial degradation rate

Photocatalyst	Apparent reaction rate constant, k_a (s^{-1})	Initial degradation rate, r_d ($mol\,l^{-1}\,s^{-1}$)
P25 suspended fine particles	1.034×10^{-4}	4.496×10^{-7}
Magnetic photocatalyst (pH 1.0)	6.073×10^{-5}	2.640×10^{-7}
Magnetic photocatalyst (pH 2.0)	4.961×10^{-5}	2.157×10^{-7}
Magnetic photocatalyst (pH 3.5)	3.878×10^{-5}	1.686×10^{-7}
Quartz sand supported TiO_2	1.442×10^{-5}	6.270×10^{-8}

Furthermore, it should be noted that the degradation efficiency of POM-based magnetic photocatalyst varies with the pH of solution, as shown in Fig. 6. It was found that acid environmental was favorable for the degradation catalyzed by POM. The initial degradation rate of formic acid over the POM-based magnetic photocatalyst increased by a factor of 1.6 as the pH of solution was lowered from 3.5 to 1.0. According to Hu and Xu [33], the dependence of the photocatalytic activity of POM anions on the pH might be associated with the partial change of the $H_3PW_{12}O_{14}$ (PW) structure from PW_{12} into PW_{11} at high pH.

To assess the apparent quantum efficiency, the remnant UV-flux outside the reaction space was measured. As shown in Table 2, a remnant UV-flux was detected outside the UV-monitor window, indicating that a fully irradiated photoreaction (FIP) condition was achieved for all degradations. As a first observation, the quartz sand supported TiO_2 has the highest power capture (99.4%) of incident UV-flux among all photocatalysts. P25 particles showed a power capture of 92.7%. Apparent power captures ranged from 87.6% to 88.3% were obtained for the POM-based magnetic photocatalyst, which is the lowest among the three photocatalysts.

Apparent quantum efficiency and energy efficiency was calculated and shown in Table 2. P25 fine particles exhibited the highest apparent quantum efficiency of 12.5% among all degradations. This result is somewhat higher than these results reported by other studies, which are usually under 10% [35,36]. The higher apparent quantum efficiency was ascribed to the low TiO_2 (P25) concentration used in this study. In order to ensure the FIP condition, a P25 concentration of 0.024 $g\,l^{-1}$ is used in this study, while P25 photocatalyst concentrations reported in other studies ranged from 1 to 8 $g\,l^{-1}$. Under the FIP condition, lower concentration of TiO_2 fine particles in reaction space leads to a lower extent of back-scattering and reflecting. This was well supported by Serpone [17] that they studied the effect of TiO_2 concentrations on apparent quantum yield and found the appar-

Table 2
Results of UV intensity measurements, apparent quantum efficiency and energy efficiency

Photocatalyst	Remnant UV-flux intensity (I_{out}) (mW cm^{-2})	Remnant UV power (P_{out}) (W)	Apparent power capture (P_a%)	Apparent photon capture rate (r_{ph}) (einstein s^{-1})	Apparent quantum efficiency (η_a%)	Energy efficiency (EED) (ppm kw^{-1} h^{-1})
Degussa P25 fine particles[a]	0.254	0.592	92.7	1.592×10^{-5}	12.5	9199.1
Magnetic photocatalyst[a,b]	0.405	0.944	88.3	1.517×10^{-5}	6.90	5402.9
Magnetic photocatalyst[a,c]	0.431	1.005	87.6	1.504×10^{-5}	6.36	4412.7
Magnetic photocatalyst[a,d]	0.414	0.965	88.1	1.512×10^{-5}	4.99	3450.1
Quart sand supported TiO_2[a]	0.022	0.051	99.4	1.706×10^{-5}	1.84	1282.9

[a] Incident UV-flux intensity (I_{in}) = 8.390 mW cm^{-2} and incident UV power (P_{in}) = 8.093 W.
[b] Reaction solution with pH 1.0.
[c] Reaction solution with pH 2.0.
[d] Reaction solution with pH 3.5.

ent quantum yield increased from 1.1% to 21.5% as the TiO_2 concentration decreased from 4 to 0.10 g l^{-1}.

The supported TiO_2 photocatalyst shows 6.8 times lower apparent quantum efficiency than that of P25 fine particles. This significant loss in quantum efficiency is induced by the lower initial reaction rate and larger particle sizes of the quartz sand supported TiO_2. Eq. (4) indicates that a lower degradation rate is directly associated with lower apparent quantum efficiency at a fixed apparent power capture of UV-flux. On the other hand, it is known that large particles induce serious scattering and reflection loss of UV-flux, which subsequently lead to low quantum efficiency.

Similar to the degradation rate results, the POM-based magnetic photocatalysts showed intermediate apparent quantum efficiency between P25 fine particles and supported TiO_2. Due to the variation of initial reaction rates, the quantum efficiency changes with the acidity of water solution. The highest apparent quantum efficiency of 6.90% was obtained at pH 1.0, which is 1.8 times lower than P25 fine particles and 3.8 times higher than the quartz sand supported TiO_2 photocatalyst. The higher degradation rate and quantum efficiency of the POM-based magnetic photocatalyst ensured its applicability for practical use.

Additionally, the energy efficiency was calculated for each degradation system. The energy efficiency could be used as a convenient reference for the evaluation of economical feasibility of each photocatalytic reacting system. The ratio of apparent quantum efficiency to the energy efficiency could be used to examine the power utilization of the reacting system and optimize reactor configuration and photocatalyst loading. The energy efficiency results in Table 2 indicated that the POM-based magnetic photocatalyst (5402.9 ppm kw^{-1} h^{-1} at pH 1.0) had a significantly higher (4.2 times) energy efficiency than the supported TiO_2 photocatalyst (1282.9 ppm kw^{-1} h^{-1}), although lower than the P25 fine particles (9199.1 ppm kw^{-1} h^{-1}).

4.3. Magnetic separation

4.3.1. Particle capture capacity

Finite element analysis (FEA) was employed to simulate the magnetic field intensity/gradient distribution in the HGMS. Simulations were carried out by FEMM 4.0 (Foster–Miller Inc.). The HGMS separation chamber was simplified as a 2D static magnetic filed because the width of separation chamber (40 mm) was smaller than that of magnet (50.8 mm). As indicated later (Fig. 7(b)), this could ensure a fairly uniform magnetic field in the width direction (z-direction in Fig. 2). All simulations were conducted under an open boundary approximation with an asymptotic boundary [37]. The results of the magnetic field distribution in the separation chamber before and after packing the fine-grade stainless steel wires were shown in Figs. 7 and 8, respectively.

From Fig. 7(a), it is observed that a fairly uniform magnetic filed exists in the space between magnets. The magnetic field (H) data at the boundaries (i.e., left and right walls, $x = \pm 10$), the center axis ($x = 0$), and the positions between the center and walls ($x = \pm 5$) of separation chamber were plotted in Fig. 7(b). y is the distance from the bottom of magnets as shown in Fig. 2 (y = 10–90 mm for the separation chamber section). It was shown in Fig. 7(b) that, despite of the remarkable variances near the top and bottom regions of the separation chamber, i.e., y = 10–20 and y = 80–90 mm, an analogously constant magnetic field with the magnitude of 2.3×10^8 A m^{-1} exists in most area of the separation chamber. Hence, the height range between y = 20 mm and y = 80 mm in the separation chamber was considered as a "constant H region" with the magnetic field intensity of 2.3×10^8 A m^{-1}.

The dehomogenized magnetic field in the wire matrix was shown in Fig. 8(a). A new Cartesian coordinate designated as x'–y' was created to avoid confusion with the coordinate in Fig. 2. The packing of wires was idealized to be uniform. Line A, B, C, B′ and A′ were chosen as typical positions in the voidage space to investigate the magnitude of the generated magnetic field gradients. Fig. 8(b) shows that the generated magnetic field gradient (dH/dr) ranged from 5.46×10^{12} to 1.68×10^{14} A m^{-2}. The $(dH/dr)_{min}$ gives the minimum traction force exerted on particle.

For the magnetic photocatalyst particles, the average diameter of particle aggregates was determined to be 650 nm by DLS. In terms of the magnetic hysteresis loop shown in Fig. 4, the magnetization of magnetic photocatalyst particles already reached saturated magnetization (46.1 A m^2 kg^{-1}) when the external magnetic field is higher than 10^6 Am^{-1}. Since the generated magnetic field is far higher in the separation chamber (see Fig. 7(b)), the magnetization of particles was kept at the sat-

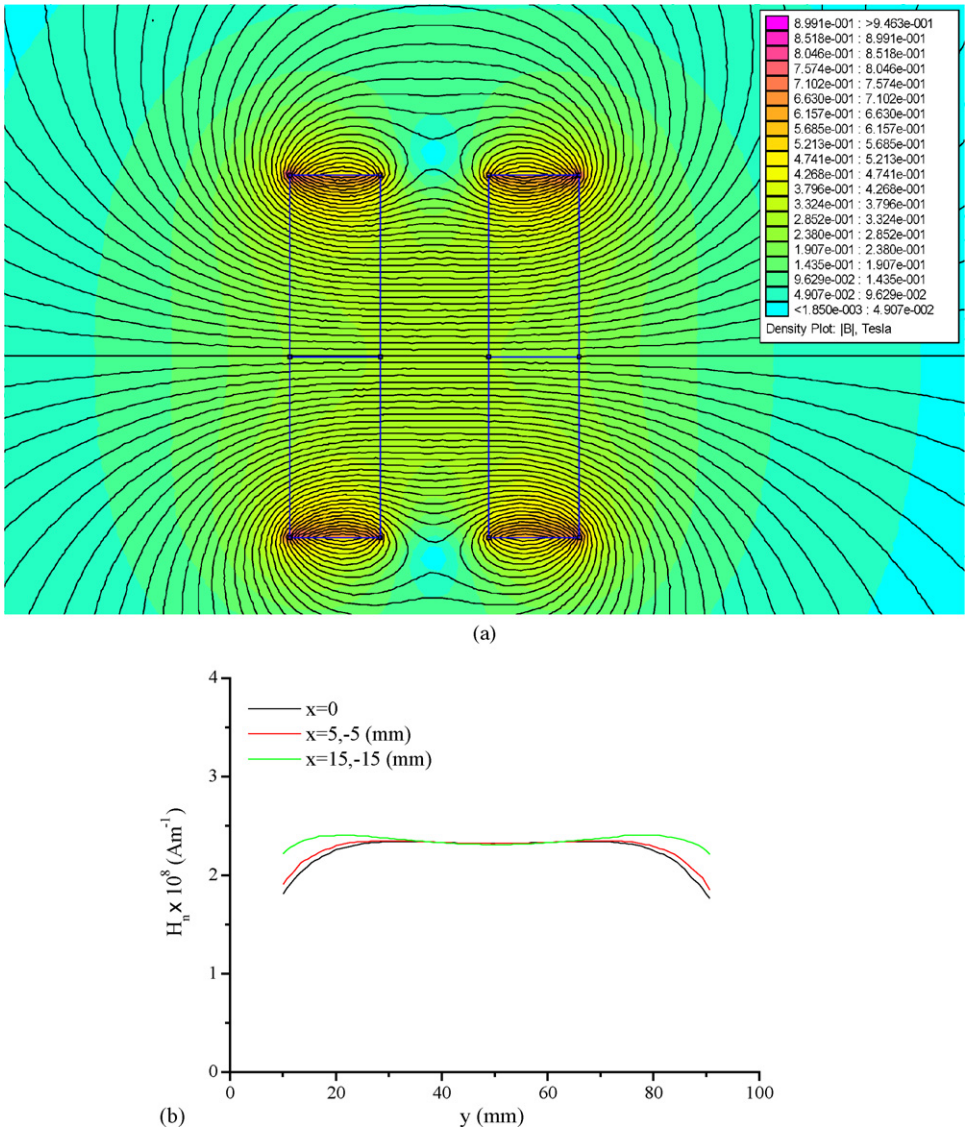

Fig. 7. Magnetic field distribution in HGMS separation chamber.

urated value during the separation. By substituting these values and $(dH/dr)_{min}$ in Eq. (10), a minimum magnetic traction force with a magnitude of 5.50×10^{-9} N was obtained for magnetic photocatalyst particles.

In terms of Eq. (11), the fluid drag force on particles was dependent on its relative velocity to fluid. In this study, magnetic particles were assumed to have no relative motion with fluid at *y*-axis, i.e., they move at the same velocity as the fluid in *y*-direction. Since the relative motion only occurs on *x*-axis, the term "*u*" in Eq. (11) actually designates the relative velocity of particles with fluid on *x*-direction ($u_{r,x}$). The calculation of fluid drag force may become rather complicated because $u_{r,x}$ was affected by magnetic traction force that is strongly position-dependent without a good definition, as shown in Fig. 8(b). However, within the flow range of $10^{-4} < Re < 0.2$, a magnitude of 1.88×10^{-9} to 9.42×10^{-13} N was obtained by using Eq. (11). These results preliminarily predict the feasibility for the magnetic photocatalyst separation by using the lab-constructed HGMS since the minimum magnetic traction force was three times larger than fluid drag force. Furthermore, it should be noticed that, as magnetic particle approaches wire, the magnetic traction force becomes larger, which will result a higher fluid drag force due to the acceleration. In other words, the magnetic traction force will increase as the fluid drag force increases, which further ensured the argument that magnetic force dominates the forces on particles in the entire approaching process.

4.3.2. Separation experiments

The separation efficiency is affected by fluid velocity because the retention time of particles in the HGMS depends on the fluid flow velocity. Therefore, separation experiments were conducted at different flow velocities to investigate the influence of fluid velocity on the separation efficiency. Separation experiments at each flow velocity were conducted for 60 min continuous operation to examine the magnetic separation capacity of HGMS. Three flow velocities, 0.688, 1.375 and 3.440 mm s^{-1}

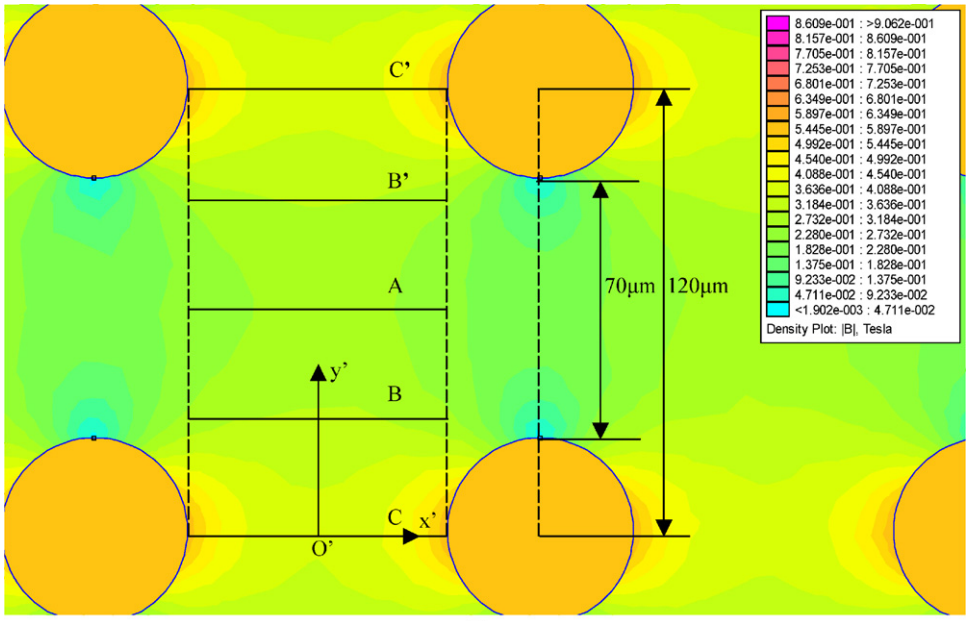

(a)

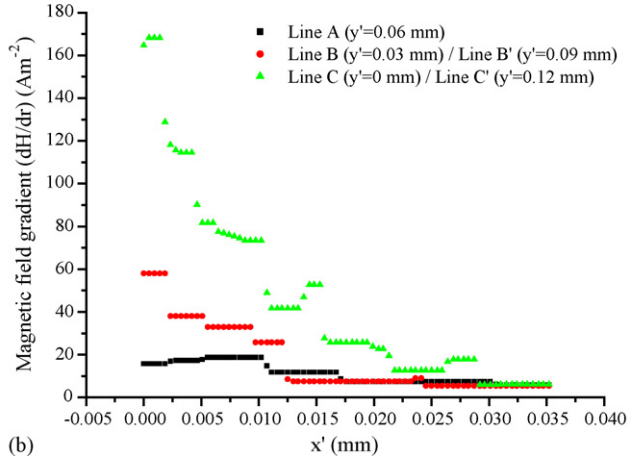

(b)

Fig. 8. Magnetic field gradients around fine-grade stainless steel wires.

were chosen, which give a retention time of approximately 2, 1 and 0.4 min for magnetic photocatalyst particles, respectively. Fig. 9 shows the separation results at three different flow velocities.

As seen from Fig. 9, steady separation performance in 60 min continuous operation was observed at the flow velocity of 0.688 and 1.375 mm s^{-1}, which is due to the synergic effect of low particle concentration (0.012 wt.%) in treated water and the low fluid flow velocity applied. At the lowest flow velocity, i.e., 0.688 mm s^{-1}, the separation efficiency kept at 95.4% with minor fluctuations. A threshold fluid velocity of 1.375 mm s^{-1} was found for maintaining the separation efficiency higher than 90.1%. It was shown that the separation efficiency decreased to 90.1–95.2% at the flow velocity of 1.375 mm s^{-1} with a slightly decreasing trend as the separation proceeded. As flow velocity increased to 3.440 mm s^{-1}, the separation efficiency remarkably decreased to 60.4–75.3% in 60 min continuous operation with an obvious decreasing trend. The experimental results suggest a strongly dependence of the magnetic separation efficiency

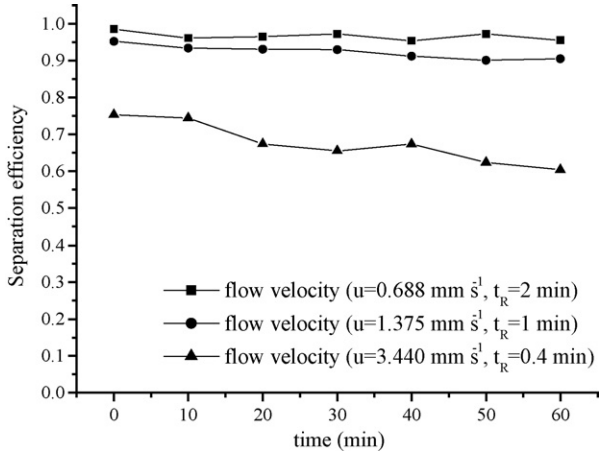

Fig. 9. Magnetic separation results.

on the particle retention time inside the HGMS. Also, it confirmed that the novel POM-based magnetic photocatalyst could be efficiently separated from treated water by using HGMS and controlling the flow velocity.

5. Conclusion

A novel POM-based magnetic photocatalyst was assessed and compared to the conventional suspended P25 fine particles and supported TiO_2 photocatalysts with respect to the degradation rate, apparent quantum efficiency and energy efficiency. Though lower than P25 fine particles, the apparent quantum efficiency of the magnetic photocatalyst was 2.7–3.8 times higher than quartz sand supported TiO_2, depending on the pH of solution. At three pH levels involved in this study (pH 1.0, 2.0 and 3.5), it exhibited the highest initial degradation rates at pH 1.0, which is nearly 1.6 times higher than the lowest degradation rate at pH 3.5. By using a lab-constructed HGMS, the magnetic photocatalyst particles were efficiently separated from treated water, with the separation efficiency higher than 90.1% at the flow velocity lower than 1.375 mm s^{-1} under the studied magnetic photocatalyst loading.

Acknowledgements

The authors gratefully appreciate the financial support from NSERC and NBIF.

References

[1] A. Fujishima, T.N. Rao, D.A. Tryk, Titanium dioxide photocatalysis, J. Photochem. Photobiol. C: Photochem. Rev. 1 (2000) 1–21.
[2] S.A. Lee, K.H. Choo, C.H. Lee, H.I. Lee, T. Hyeon, W. Choi, H.H. Kwon, Use of ultrafiltration membranes for the separation of TiO_2 photocatalysts in drinking water treatment, Ind. Eng. Chem. Res. 40 (2001) 1712–1719.
[3] R.L. Pozzo, J.L. Giombi, M.A. Baltanás, A.E. Cassano, The performance in a fluidized bed reactor of photocatalysts immobilized onto inert supports, Catal. Today 62 (2000) 175–187.
[4] D. Beydoun, R. Amal, Novel photocatalyst: titania-coated magnetite. Activity and photodissolution, J. Phys. Chem. B 104 (2000) 4387–4396.
[5] D. Beydoun, R. Amal, G. Low, S. McEvoy, Occurrence and prevention of photodissolution at the phase junction of magnetite and titanium dioxide, J. Mol. Catal. A: Chem. 180 (2002) 193–200.
[6] D. Beydoun, R. Amal, Studies on the mineralization and separation efficiencies of a magnetic photocatalyst, Chem. Eng. Technol. 24 (2001) 745–748.
[7] Y.-L. Shi, W. Qiu, Y. Zheng, Synthesis and characterization of a POM-based nanocomposite as a novel magnetic photocatalyst, J. Phys. Chem. Sol., in press.
[8] A. Ditsch, S. Lindenmann, P.E. Laibinis, D.I.C. Wang, T.A. Hatton, High-gradient magnetic separation of magnetic nanoclusters, Ind. Eng. Chem. Res. 44 (2005) 6824–6836.
[9] D.R. Kelland, Magnetic separation of nanoparticles, IEEE Trans. Magn. 34 (1998) 2123–2125.
[10] H. Okada, T. Tada, A. Chiba, K. Mitsuhashi, T. Ohara, H. Wada, High gradient magnetic separation for weakly magnetized fine particles, IEEE Trans. Appl. Supercon. 12 (2002) 967–970.
[11] N.B. Jakson, C.M. Wang, J. Schwitzgebel, J.G. Ekerdt, J.R. Brock, A. Heller, Attachment of TiO_2 powders to hollow glass microbeads. Activity of the TiO_2-coated beads in the photoassisted oxidation of ethanol to acetaldehyde, J. Electrochem. Soc. 138 (1991) 3660–3664.
[12] A. Bhargava, M.F. Kabir, E. Vaisman, C.H. Langford, A. Kantzas, Novel technique to characterize the hydrodynamics and analyze the performance of a fluidized-bed photocatalytic reactor for wastewater treatment, Ind. Eng. Chem. Res. 43 (2004) 980–989.
[13] W. Qiu, Y. Zheng, A comprehensive assessment of supported titania photocatalysts in a fluidized bed photoreactor: photocatalytic activity and adherence stability, Appl. Catal. B: Environ., in press.
[14] I.K. Konstantinou, T.A. Albanis, TiO_2-assisted photocatalytic degradation of azo dyes in aqueous solution: kinetic and mechanistic investigation: a review, Appl. Catal. B: Environ. 49 (2004) 1–14.
[15] Y. Yang, Y.H. Guo, C.W. Hu, Y.H. Wang, E.B. Wang, Preparation of surface medications of mesoporous titania with monosubstituted Keggin units and their catalytic performance for organochlorine pesticide and dyes under UV irradiation, Appl. Catal. A: Gen. 273 (2004) 201–210.
[16] J.M. Hermann, Heterogeneous photocatalysis: fundamentals and applications to the removal of various types of aqueous pollutants, Catal. Today 53 (1999) 115–129.
[17] N. Serpone, Relative photonic efficiencies and quantum yields in heterogeneous photocatalysis, J. Photochem. Photobiol. A: Chem. 104 (1997) 1–12.
[18] M. Schiavello, V. Augugliaro, L. Palmisano, An experimental method for the determination of the photon flow reflected and absorbed by aqueous dispersions containing polycrystalline solids in heterogeneous photocatalysis, J. Catal. 127 (1991) 332–341.
[19] R.L. Pozzo, M.A. Baltanás, A.E. Cassano, Towards a precise assessment of the performance of supported photocatalyst for water detoxification process, Catal. Today 39 (1999) 143–157.
[20] L.W. Miller, M.I. Tejedor-Fejedor, M.A. Andreson, Titanium dioxide-coated silica waveguides for the photocatalytic oxidation of formic acid in water, Environ. Sci. Technol. 33 (1999) 2070–2075.
[21] N.J. Peill, M.R. Hoffmann, Chemical and physical characterization of a TiO_2-coated fiber optic cable reactor, Environ. Sci. Technol. 30 (1999) 2070–2075.
[22] Dexter Magnetic Technologies Inc., Magnetic Design Calculations. Chapter 4: Magnetic Design. Reference Design Manual, pp. 27–29.
[23] Magnet Sales & Manufacturing Inc., Permanent Magnet Design Guidelines, pp. 14–16.
[24] K.H.J. Buschow, F.R. de Boer, Physics of Magnetism and Magnetic Materials, Kluwer Academic/Plenum Publishers, New York, USA, 2003, pp. 75–83.
[25] C.J. Clarkson, D. Kelland, Model for calculation of capture radii of a high gradient magnetic separator at moderate Reynolds numbers, IEEE Trans. Magn. 12 (1976) 901–903.
[26] H. Okada, K. Mitsuhashi, O. Takeshi, E.R. Whitby, H. Wada, Computational fluid dynamics simulation of high gradient magnetic separation, Sep. Sci. Technol. 40 (2005) 1567–1584.
[27] G.D. Moeser, K.A. Roach, W.H. Green, T.A. Hatton, High-gradient magnetic separation of coated magnetic nanoparticles, AICHE J. 50 (2004) 2835–2848.
[28] R. Gerber, M. Takayasu, F.J. Friedlaender, Generalization of HGMS theory: the capture of ultra-fine particles, IEEE Trans. Magn. 19 (1983) 2115–2117.
[29] Degussa Corp., Product information sheet of Aeroxide TiO_2 P25 hydrophilic fume titanium dioxide, December 2004.
[30] A. Houas, H. Lachheb, M. Ksibi, E. Elaloui, C. Guillard, J.M. Hermannc, Photocatalytic degradation pathway of methylene blue in water, Appl. Catal. B: Environ. 31 (2001) 145–157.
[31] C. Su, B. Hong, C. Tseng, Sol–gel preparation and photocatalysis of titanium dioxide, Catal. Today 96 (2004) 119–126.
[32] S. Kim, H. Park, W. Choi, Comparative study of homogeneous and heterogeneous photocatalytic redox reactions: $PW_{12}O_{40}^{3-}$ vs. TiO_2, J. Phys. Chem. B 108 (2004) 6402–6411.
[33] M. Hu, Y. Xu, Photocatalytic degradation of textile dye X3B by heteropolyoxometalate acids, Chemosphere 54 (2004) 431–434.
[34] R.R. Ozer, J.L. Ferry, Photocatalytic oxidation of aqueous 1,2-dichlorobenzene by polyxometalates supported on the NaY zeolite, J. Phys. Chem. B 106 (2002) 4336–4342.

[35] N. Serpone, D. Lawless, R. Khairutdinov, E. Pelizzetti, Subnanosecond relaxation dynamics in TiO_2 colloidal sols (particle sizes $R_p = 1.0$–13.4 nm). Relevance to heterogeneous photocatalysis, J. Phys. Chem. 99 (1995) 16655–16661.

[36] G.P. Lepore, C.H. Langford, J. Vichováand, A. Vleek Jr., Photochemistry and picosecond absorption spectra of aqueous suspensions of a polycrystalline titanium dioxide optically transparent in the visible spectrum, J. Photochem. Photobiol. A: Chem. 75 (1993) 67–75.

[37] D. Meeker, User Manual of Finite Element Method Magnetics, Version 4.0., Foster-Miller Inc., 2004, pp. 73–74.